Supporting online material:

Regional synthesis of Mediterranean atmospheric circulation during the Last Glacial Maximum

J. Kuhlemann[1*], E.J. Rohling[2], I. Krumrei[1], P. Kubik[3], S. Ivy-Ochs[4], M. Kucera[1]

1. *Inst. for Geosciences, Univ. of Tuebingen, Sigwartstr. 10, D-72076 Tuebingen, Germany*
2. *School of Ocean and Earth Science, National Oceanography Centre, Southampton, SO14 3ZH, United Kingdom.*
3. *Institute of Particle Physics, HPK H30, ETH Zurich, CH-8093 Zurich, Switzerland*
4. *Institute of Particle Physics, HPK H27, ETH Zurich, CH-8093 Zurich, Switzerland*

*Correspondence to: kuhlemann@uni-tuebingen.de

Data supplement 1: Regional setting in Corsica and methodology

As shown in Figs. 1 and 2 of the main paper, the island of Corsica in the western Mediterranean basin is characterized by steep gradients of the equilibrium line altitude (ELA) and of ΔT_{ELA}. Because of these steep gradients, Corsica is considered to be a highly sensitive palaeoclimatic key area within the Mediterranean. A set of regional climatic and palaeoclimatic maps of Corsica demonstrates how recent climate differentiation compares to that of the Last Glacial Maximum (LGM). Our regional study demonstrates how strongly the equilibrium line altitude (ELA) can vary on local scales within a 150 x 50 km-sized mountain range, and how a reasonable average is extracted. For this purpose, we briefly introduce regional work and methodology of dating LGM glacier expansion which we transform to palaeoclimatic data.

Corsica is largely composed of granites that formed between 340 Ma and 280 Ma. They contain quartz suitable for exposure dating. Rhyolites in the northwest and oceanic basement with sedimentary cover rocks in the east are unsuitable for exposure dating. Rugged relief with elevations up to 2706 m in the NW of Corsica contains also palaeosurface relics up to 30 km^2 in size at the level of the summits *(S1)*. The recent climate of Corsica at sea-level is characterised by subtropical Mediterranean-type conditions (warm dry summer and temperate wet winter) whereas the montane zone between 1000 and 1800 m is characterised by temperate conditions. Above ~1800 m, subalpine to alpine climate conditions prevail. Average annual precipitation increases from c. 600 mm/yr on the coast to more than 1500 mm/yr inland *(S2)*. During the last glaciation, glaciers reached down to 500 m above present sea-level in some valleys. The extent of glaciation has been studied by air photo analysis, detailed field mapping, and valley-by-valley correlation, revising earlier regional work *(S3)*. Careful mapping is essential since only few selected sites provide proper sampling conditions for exposure dating.

To extract palaeoclimate information from the expansion of ancient glaciers in Corsica, we apply the accumulation area ratio-method (AAR) with a standard ratio of 0.6 for the size of the ablation area relative to accumulation area to map the ELA *(S4)*. ELA reconstructions are quite robust for Alpine-type mountain glaciers *(S5)*, since $\pm$100 m ELA difference means $\pm$200 m elevation difference for the tongue of typical Alpine glaciers, equivalent to $\pm$0.6 ºC temperature difference or +11 %/ -9 % precipitation difference *(S6)*. For smaller glaciers and those with a regular vertical profile and typical shape in map view, the error of the ELA calculation is $\pm$50 m, increasing to $\pm$100 m for large and complex-shaped glaciers.

LGM maximum extent of glaciers

Exposure ages (^{10}Be) for a confirmation of LGM depositional ages in Corsica are shown in Figure S1 and Tab. S1. Exposure dating is based on the assumption that rock surfaces like that of a glacial boulder or a glacially abraded basement rock in a valley floor (roche moutonnée) are totally reset (at least 2 m of rock abraded) and exposed to cosmic rays ever since melting of glaciers. As sea-level high-latitude (SLHL) ^{10}Be production rate we used a value of 5.1±0.3 atoms g^{-1} yr^{-1} with a spallation fraction of 0.978 (*S7, S8*). Local surface production rates were calculated after Stone *(S7)* using linear interpolation between decadal latitude values. Depth correction was calculated using attenuation length values of 155 g cm^{-2} and 1510 g cm^{-2} for spallation and muons, respectively, and assuming downward exponential decrease of nuclide production *(S8)*.
Exposure ages of glacial boulders are corrected for topographic shielding. The shielding values were derived from a high-resolution Digital Elevation Model (DEM). Elevation and latitude were determined from French IGN 1:25000 topographic maps. The exposure ages are not corrected for cover of vegetation, snow or sediment, since in the mid-elevation sampling sites their effects are negligible. We have corrected for the variation of the geomagnetic field in the past on the cosmogenic ^{10}Be production *(S9)*, and calculated the fully propagated 1□-error of our data. Postglacial weathering, depending on local climate and lithology with a certain range of error, has also been considered for age calculation as independent control of weathering rates is available *(S1)*. Purified quartz samples of 13 to 46 grams were prepared for Accelerator Mass Spectrometry (AMS) at ETH Zurich. The measured ^{10}Be/^{9}Be ratios were normalized to the standard S555 with a nominal value of 95.5^{-12} using a ^{10}Be half-life of 1.51 Myr. The results show ages scattering between ~14 and ~28 kyrs, which match with the LGM (18-24 kyrs) within the range of error (Table S1; Figure S1, frame of the map shown in Figure S3c). A “too old” age (Ku119) reflects that less than 2 m of granite were eroded from a glacial boulder and the rock kept a ^{10}Be relict of pre-exposure from previous time of cosmic radiation. A “too young” age of a boulder (Ku51) reflects either tilting of a glacial boulder or a shielding sediment cover.

Tab. S1: Results of exposure dating

No.	lat. [°] N	long. [°] E	alt. [m]	Qz [g]	10^4 Be [at g^{-1}]	analyt. error [%]	topogr. shield.	sample thick.[a] [cm]	local prod. rate [at g^{-1} yr^{-1}]	geomag. corr.	erosion rate[b] [mm kyr^{-1}]	age [kyr] incl. erosion	age [kyr] no erosion	error [kyr] incl. SLHL no erosion
Ku29	42,28	9,11	640	42,20	19,10	5,1	0,978	4	8,10	1,04	3	**24,9**	**23,3**	2,9
Ku37	42,20	8,92	1120	15,65	19,77	4,7	0,997	2	12,30	1,01	10	**18,2**	**15,6**	1,9
Ku47	42,03	9,19	1460	13,51	29,96	4,3	0,997	2	15,89	1,02	10	**21,9**	**18,2**	2,2
Ku51	42,02	9,11	1260	33,35	16,90	8,5	0,986	3	13,40	1,00	10	**13,8**	**12,3**	1,7
Ku52	42,02	9,11	1250	23,20	22,65	6,3	0,986	2	13,41	1,01	10	**19,2**	**16,3**	2,1
Ku84	41,87	9,18	1465	17,91	31,26	4,2	0,999	2	15,94	1,02	10	**22,9**	**18,9**	2,3
Ku86	42,15	9,06	1070	18,37	18,24	6,4	0,950	3	11,17	1,01	10	**18,0**	**15,5**	2,0
Ku90	42,30	8,90	1210	45,60	20,15	8,1	0,993	4	12,93	1,01	10	**17,3**	**14,9**	2,1
Ku91	42,30	8,90	1230	14,52	23,38	6,6	0,993	1	13,45	1,01	10	**20,1**	**17,0**	2,2
Ku103	42,11	9,12	1190	16,56	20,30	7,8	0,980	2	12,74	1,01	10	**17,0**	**14,7**	2,0
Ku110	42,12	9,12	1110	23,07	21,34	8,9	0,989	3	11,99	1,01	15	**21,7**	**16,6**	2,4
Ku111	42,12	9,12	1130	17,87	18,74	10,8	0,985	3	12,13	1,01	15	**18,0**	**14,4**	2,2
Ku112	42,12	9,12	1115	24,15	20,02	11,8	0,983	3	11,97	1,01	15	**19,9**	**15,5**	2,5
Ku117	42,01	9,23	1405	17,17	25,57	4,8	0,988	2	15,11	1,01	10	**19,2**	**16,3**	2,0
Ku119	42,28	8,93	1170	15,67	28,12	15,6	0,992	2	12,74	1,03	10	**26,6**	**21,3**	4,0
Ku125	42,28	9,01	1553	20,13	27,73	4,7	0,995	3	16,91	1,01	10	**18,7**	**15,9**	2,0
Ku127	42,28	9,02	1538	22,62	25,21	5,8	0,996	3	16,74	1,00	10	**16,9**	**14,6**	1,9
Ku138	42,28	9,01	1575	20,33	31,80	5,5	0,997	2	17,36	1,00	10	**21,1**	**17,6**	2,2

[a]: estimated error of sample thickness ± 0.5 cm
[b]: assumed error of erosion rate 50 %

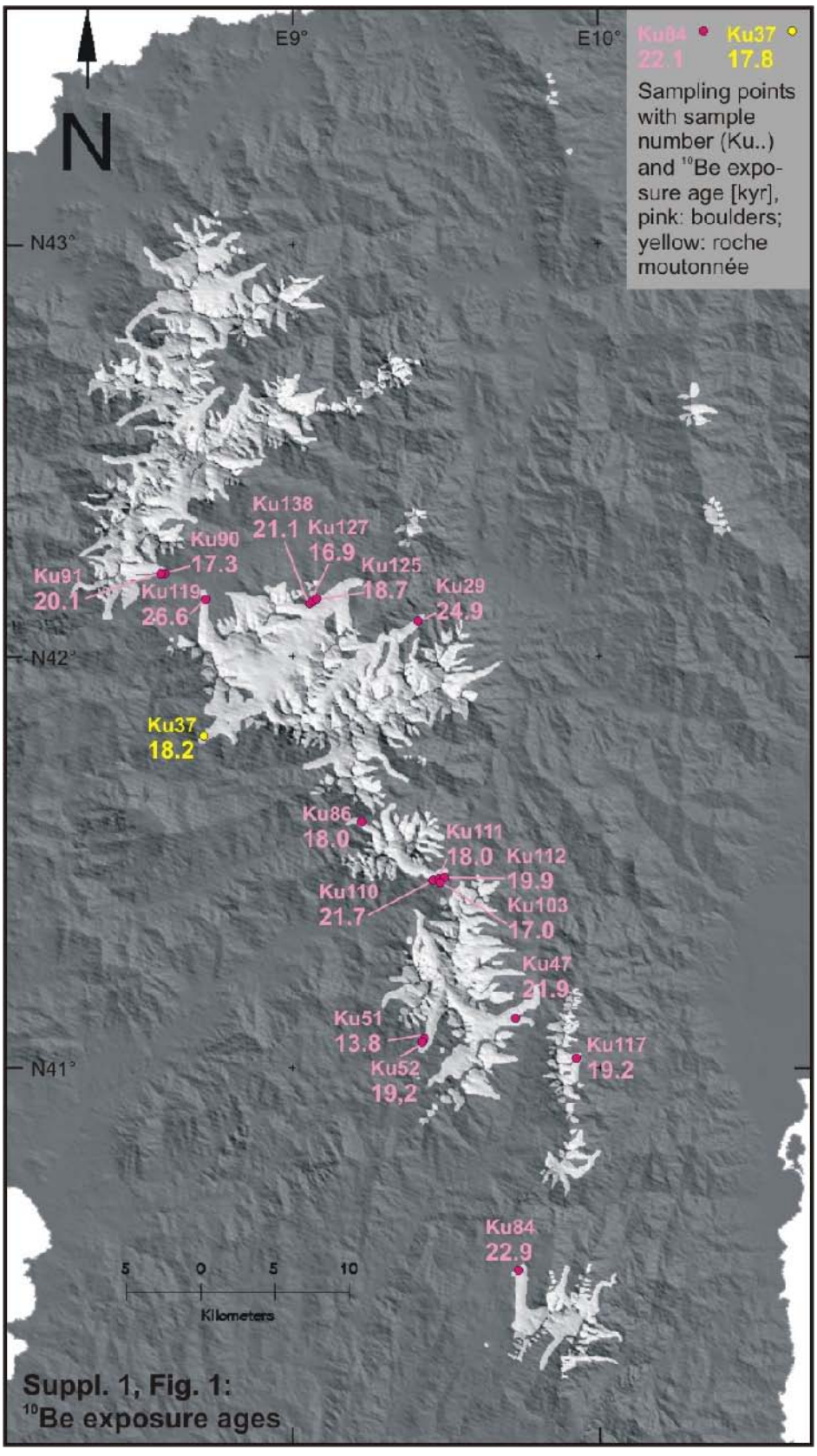

Figure S1: Distribution of glaciers in Corsica during the LGM and location of samples for exposure ages.

Present climate and differentiation of temperature and precipitation effects on the ELA

We have calculated precipitation and temperature differences from average values,(*S2*) to highlight regional anomalies. These Present regional anomalies will be compared with those of the LGM below.

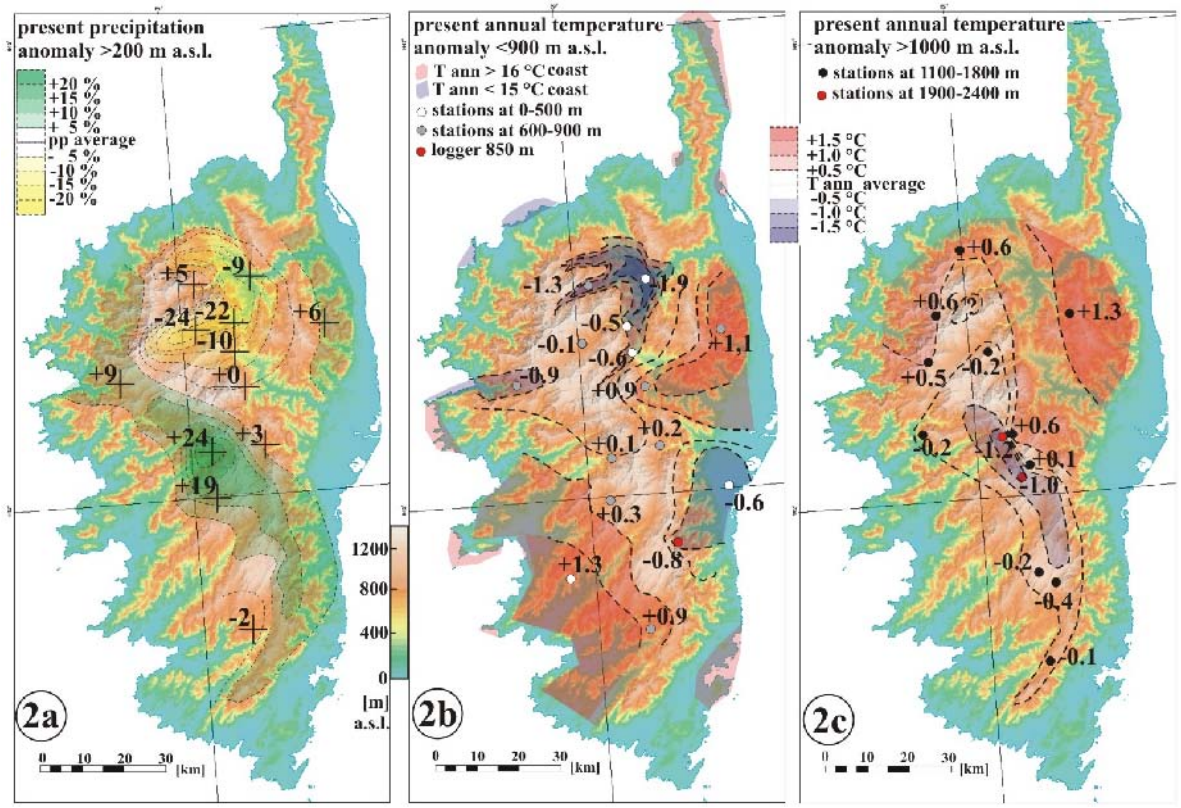

Figure S2: Present-day anomalies of precipitation (S2a), low-elevation (Mediterranean climate; S2b) and high-elevation (montane to alpine climate; S2c) annual temperatures.

The precipitation anomaly at Present (Figure S2a) is calculated as the difference (%) to the mean elevation-dependent regional precipitation rate which is f (pp) = 600 mm yr^{-1} (+ 640 mm km^{-1} yr^{-1}), valid up to ~1000 m a.s.l. (highest meteorological stations), calculated for a reference level of 700 m (most stations). Above ~1000 m a.s.l. no reliable measurements are available and such measurements are difficult because of strong winds during periods of precipitation. The empiric function of elevation-dependent precipitation is calculated from data of meteorological stations (*S2*) marked in Figure S2a.

The temperature anomaly (Figure S2b,c) is calculated as the difference from the temperature (°C) computed from the free atmospheric lapse rate of 6.5°C km^{-1} and 15.5 °C average annual temperature close to sea level *(S2)*. In Figure S2b, the annual average temperature of each meteorological station (*S2*) is compared to the elevation-dependent annual average temperature to be expected from the lapse rate of 6.5°C km^{-1} and 15.5 °C at sea level, and the difference is further treated as an anomaly. In Figure S2c this is done for averages obtained at elevations above 1000 m a.s.l., obtained by automatic loggers between 2003 and 2007 (own monitoring programme).

Today, anomalies of low-elevation annual temperature indicate that relatively warm air is advected from the SW and NE, whereas in the northern central interior temperature inversions indicate semi-continental local conditions.

Modern ELA relationship for Corsica

The anomalies calculated from present day regional averages of annual temperature and precipitation, based on climate station records *(S2,* see above*)*, are now used to construct a map of the present (1960-1990 climate normal) local ELA variability. Finally, inverse application of this method provides a first-order differentiation of the ELA anomaly of the LGM into precipitation and temperature anomalies for that time (see below).

For ELA studies in Corsica, temperatures at higher elevation in well-mixed air masses show a relatively warm north and a cool south-central ridge (Figure 2c), which coincides with a positive precipitation anomaly (Figure 2a).

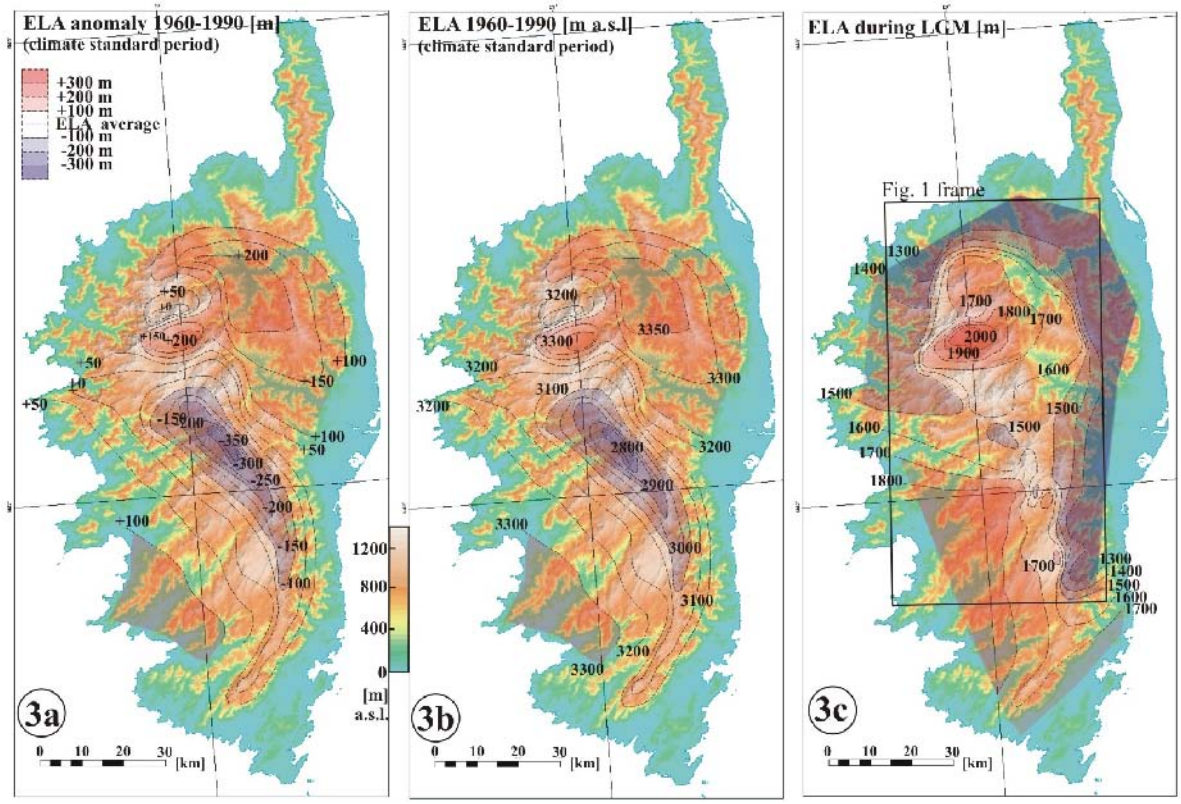

Figure S3: Present ELA anomaly in meters differing from the average ELA (S3a), and both Present (S3b), and LGM (S3c) ELA in meters above *present* sea-level

The empirical relationship of temperature versus precipitation of temperate Alpine-type glaciers at the ELA *(S6)* is used to integrate the present ELA. At about 1500 to 2000 mm of annual precipitation, ±1 ºC summer temperature change is equivalent to +18 %/ -15 % precipitation change *(S6,S10)*.

Figure S3 shows a recent ELA anomaly pattern that is calculated from the combination of the temperature and precipitation anomaly distributions shown in Figures S2a and S2c, assuming 100 m ΔELA equivalent to 0.65 ºC ΔT, and 100 m ΔELA equivalent to +11 %/ -9 % of Δ precipitation (*S6*; Figure S3a).

In Figure 3b, the ELA anomaly pattern of Figure 3a is added to a mean ELA position of 3150 m, which provides a regional ELA map. We estimated the mean ELA of 3150 m for the standard climate period (1960-1990) temperature records since 2003 at the summits, which have to be corrected for climate warming that occurred during the last decades to give appropriate 'pre-industrial' estimates. A ~250 m ELA rise in the last 20 to 30 years is estimated from: (1) a rise of the tree line by ~150 m that is reflected by a zone of juvenile trees and that is largely driven by temperature (*S11*), and (2) ~100 m ELA rise associated with a 10 % precipitation decrease during the period 1991-2000 relative to 1960-1990 (west coast-near station of Ajaccio; *S12*).

Warm and dry local climate causes a positive ELA anomaly (high ELA) whereas cool and wet local climate causes a negative ELA anomaly (low ELA). Figures S3a and S3b reveal a local ELA range of 550 ±50 m within the fairly small island of Corsica. A positive anomaly is observed in the northern interior as a result of foehn effects *(S1)*. The climatic reason of the negative ELA anomaly (Figure S3a) – i.e., the ELA depression to 2800 ±50 m (Figure S3b) – in southern-central Corsica is not known in detail. One major reason will be regional topography, with only one prominent drainage divide and frequent precipitation that is governed by daily land-sea circulation and insolation-driven convection during the warm season. Another likely reason would be that larger-scale atmospheric circulation exposes southern-central Corsica to subtropical disturbances more than northern Corsica. In addition, southern Corsica is rather densely covered by (deciduous) forest, supporting local recycling of moisture. A recent negative ELA anomaly in south-central Corsica is confirmed by moisture data from loggers, amounts of snowfall over the last 5 years, and the pattern of the temporal snowline and vegetation belts, as compiled from remote sensing, monitoring, and field observations (*S1*). Within this zone, snow patches occasionally survive through the summer in cirques at elevations down to 2100 m. In the same cirques, there is evidence of niche glaciers during the Little Ice Age *(S3)*.

Last Glacial Maximum ELA in Corsica

The range of spatial variability in the ELA anomaly for the LGM in Corsica is even stronger than the modern 550 ±50 m, and was increased up to 700 m (Figure S3c). Similar to the modern pattern, the LGM pattern shows a positive anomaly in the northern centre, which is likely due to an enhanced foehn effect of NW winds. Conversely, the LGM pattern of the ELA shows a stronger (warmer) positive anomaly in the southwest and a negative (cold) anomaly at the eastern, northern, and northwestern margins. Thus, the climatic conditions at the margins of the island appear to differ considerably between the LGM and the

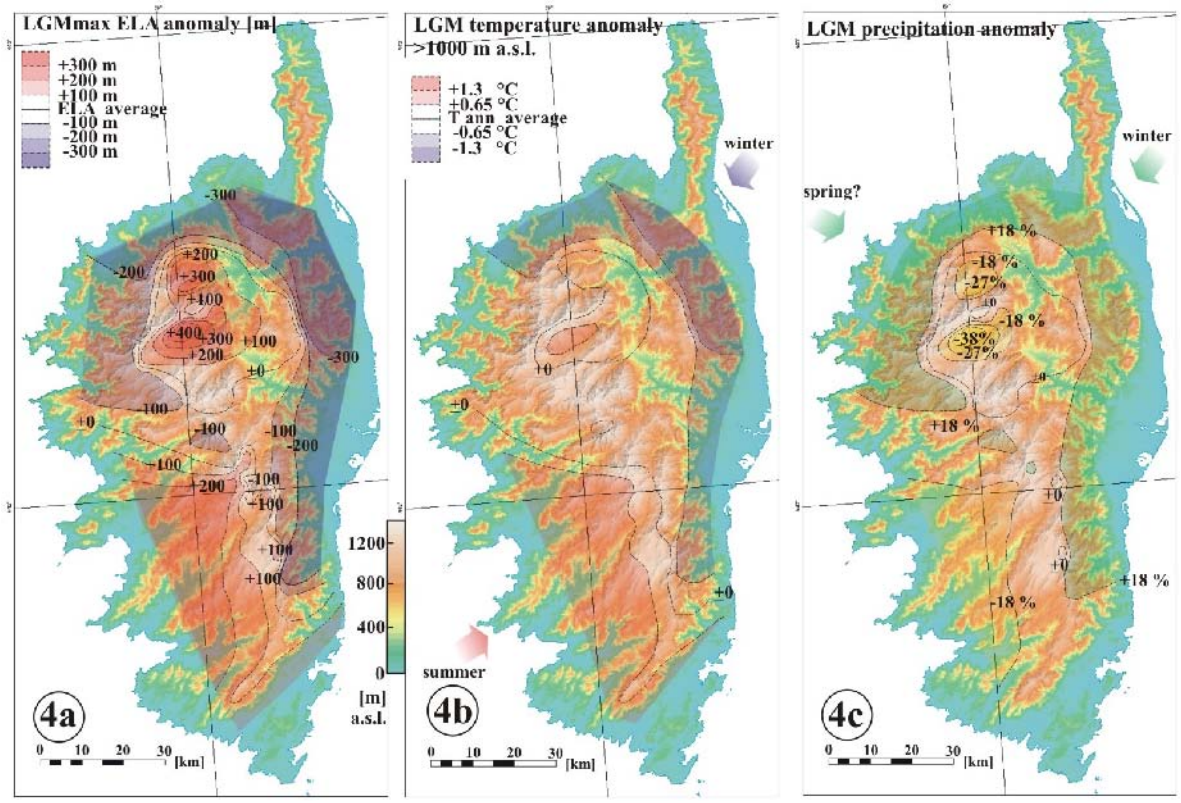

Figure S4: Last Glacial Maximum ELA anomaly (S4a), and inferred anomaly patterns of temperature (S4b), and precipitation (S4c).

Present. This needs to be explained by larger scale atmospheric circulation, which is the focus of the main paper.

Figure S4a converts the ELA of the LGM shown in Figure S3c into an anomaly map, by subtracting the LGM mean ELA value of 1600 m. Application of the inverse of the arguments described above then allows for a first-order deconvolution of the underlying temperature and precipitation components (Figures S4b and S4c). In the NE, a stronger temperature component reflects winter-time (very cold) continental air advection from the N and NE (see also main text; Figure S4b). In the northern centre, a stronger moisture deficit reflects reduced recycling of moisture from reduced vegetation cover (no forest), and inferred changes of larger scale atmospheric circulation (Figure S4b). In the NW, we infer a dominant precipitation component in analogy to a modern positive spring-time precipitation anomaly (*S2*). Relatively high temperatures in the SW of Corsica both at present (at altitudes up to 900 m; Figure S3a,b) and in the LGM (Figure S4b) may reflect advection of relatively warm and seasonally dry air from the western Sahara, predominantly during summer. However, it may also reflect easterly advection of cold and humid air in winter, associated with stationary or slowly moving cyclones in the northern Tyrrhenian Sea, which cause foehn effects in the SW of Corsica. Such a synoptic situation has been reported several times in recent winters, and we infer that it may have been more frequent during the LGM, given that the SW Corsican warm anomaly appears to have been more pronounced during the LGM as compared to the Present.

References:
S1 J. Kuhlemann, K. van der Borg, M. Danišík, W. Frisch, *Int. J. of Earth Sci.*, doi: 10.1007/s00531-007-0169-z (2007).
S2 C. Bruno, G. Dupré, G., Giorgetti, J.P. Giorgetti, J. Alesandri, "Météorologie, climat et microclimates de la Corse" *CNDP-CRDP de Corse/ Météo France*, 138 pp., Ajaccio, France (2001)
S3 J. Kuhlemann et al., *Austrian J. Earth Sci.* **97**, 68 (2005).
S4 S.C. Porter, *Quat .Sci . Rev.* **20**, 1067 (2001).
S5 H. Kerschner, G. Kaser, R. Sailer, *Ann. Glaciol.* **31**, 80 (2000).
S6 A. Ohmura, P. Kasser, M. Funk, *J. Glaciol.* **38**, 397 (1992).
S7 G. Balco, J.O. Stone, N.A. Lifton, T. J. Dunai. *Quat. Geochron.,* doi:10.1016/ j.quageo.2007.12.001 (2008).
S8 J. Stone *J. Geophy. Res.* **105,** 23,753 (2000)
S9 J. Pigati, N. Lifton, *EPSL* 226, 193-205 (2004)
S10 P.D. Hughes, J.C. Woodward , P.L. Gibbard, *EPSL* **253**, 50 (2007).
S11 G.-R. Walther, S. Beissner, C.A. Burga, *J. Veg. Sci.* **16**, 541-548 (2005).
S12 GHCN Global Historical Climatology Network

Data supplement S2: Mediterranean ELA during the Last Glacial Maximum (LGM)

In S2 we compile ELA information for the LGM in the wider Mediterranean from the literature, to complement our own data from Corsica (data supplement S1). Currently available ELA reconstructions for the maximum glaciation in Iberia, Italy, and the southern Dinarides (mainly Greece) lack precise chronology to pin it to the LGM, but for the Alps it is known that the maximum extent of glaciers occurred simultaneously with that of the northern hemisphere in the LGM *(S14)*. In much of Corsica, our own studies have shown that the ELA during the LGM generally was situated about 100 m higher than during the maximum glacier extent which occurred earlier in the last glacial cycle, but the LGM advance was the strongest in the southern part of the island. Also in the northern Pyrenees, glaciers were less far extended during the LGM than during earlier phases in the last glacial cycle *(S15)*, and this seems to apply throughout Iberia *(S16,S17)*. In the Southern Carpathians, some evidence exist for a stronger advance earlier in the last glacial cycle as well *(S18)*. In northern Greece, maximum glacier extent in the last glacial

cycle occurred during the LGM *(S19,S20)*. Older ELA maps for Greece and southern Italy show the maximum expansion in the last glacial cycle *(S21)*, not necessarily strictly within the LGM *(S22)*.

Table S2 shows regional work that has been performed after the earlier compilation of Messerli *(S13)*, who analysed and compiled all relevant older publications. The table and the reference list give priority to most recent regional work where older references for the particular region are noted. Special priority is given to publications which include geochronological dating of glaciers advances. So far, these are scarce.

References:

S13 D. Florineth, C. Schlüchter, *Quat. Res*. **54**, 295 (2000).
S14 M. Reille, V. Andrieu, V., *Vegetation History and Archeobotany* **4**, 1 (1995).
S15 J.M. García-Ruiz, B.L. Valero-Garcés, C. Martí-Bono, P. González-Sampériz, *J. Quat. Sci.* **18**, 61 (2003).
S16 A. P. Alberti, M.V. Diaz, R.B. Chao, in J. Ehlers, P.L. Gibbard (Eds.), *Quaternary Glaciations – Extent and chronology Part I. Europe* **2**, 389, Elsevier (2004).
S17 A. Reuther et al. *Quaternary International* **164***,* 151 (2007).
S18 P.D. Hughes, J.C. Woodward , P.L. Gibbard, *Global Planet. Change* **50**, 83 (2006).
S219 P.D. Hughes, J.C. Woodward , P.L. Gibbard, *EPSL* **253**, 50 (2007).
S20 F. Boenzi, G. Palmentola, *Zeitschr. f. Geomorph. N.F. Suppl.* **41**, 21 (1997).
S21 C. Giraudi, C., in J. Ehlers, P.L. Gibbard (Eds.), *Quaternary Glaciations – Extent and chronology Part I. Europe* **2**, 215 (2004).

Table S2:

region	mountain range	massif	latitude	long	peak alt. [m]	ELA Wuermian			Ref.
			[°] N	[°]		Early	LGM	CRN	
Spain	Galician M.	Sierra del Faro	42°17'	8°15' W	1129	900			*(S22)*
	Galician M.	Sierra Cabrera	42°10'	6°46' W	2012	1500- 1700			*(S22)*
	Cord. Cantabrica	Sierra de Picos	42°49'	6°50' W	1923	1400			*(S22)*
	Cord. Cantabrica	West	43°04'	6°09' W	2417	1450			*(S22)*
	Cord. Cantabrica	East	43°01'	4°44' W	2615	1500			*(S22)*
	Cord. Iberica	Sierra Demanda	42°08'	2°58' W	2305	1900-1950			*(S22)*
	Cord. Iberica	Sierra Moncayo	41°46'	1°50' W	2316	1950			*(S22)*
	Sistema Central	Sierra Gredos	40°15'	5°24' W	2592	1800-1850			*(S22)*
	Sistema Central	Sierra Guadarrama	40°58'	3°41' W	2469	2000			*(S22)*
	Sierra Nevada		37°03'	3°19' W	3481	2500			*(S22)*
	Pyrenees	Aneto (Maladetta)	42°33'	0°59'	3404	1700-1800			*(S23)*
	Pyrenees	Mt Perdu	42°41'	0°01'	3355	1700-1800			*(S23)*
France	Pyrenees	Carlit	42°37'	1°54'	2921	1600 - 2200			*(S23)*
	Pyrenees	Aston	42°41'	1°40'	3141	1700-1800			*(S23)*
	Pyrenees	Arres d'Anie	42°53'	0°44' E	2504	1500			*(S23)*
	Pyrenees	Ossau	42°48'	0°23' E	2884	1500			*(S23)*
	Pyreness	N Pyrenees	43°00'	0°45' E	2000	1400			*(S23)*
	Pyrenees	Canigou	42°31'	2°27'	2785	1600 - 2200			*(S23)*
	Pyrenees	Néouvielle	42°50'	0°07' E	3091				*(S23)*
	Vosges		48°02'	6°52' E	1424	900	1100	14C	*(S24)*
	Massif Central	Mont-Dore	45°34'	2°50'	1886		1000-1200		*(S25,26, 27)*
	Massif Central	Cantal	45°05'	2°45'	1858		1000-1200		*(S26, 27,28,29)*
	Massif Central	Aubrac	44°38'	3°00'	1471		1250		*(S26,27)*
	Massif Central	Forez	45°34'	3°51'	1640		1280		*(S25)*
	Jura	French Jura	46°30'	5°50' E	1723		1000		*(S26,27)*
	Corsica	N + E margin	42°	9°	1971		1400	10Be	*this paper*

	Corsica	N central	42°	9°	2706		1900	10Be	*this paper*
Helvetia	Alps	Rhine glacier	47°36'	9°25' E	3614		950		*(S30)*
Italy	Apennine	northern part	44°17'	10°24'	2165		1400		*(S31)*
	Apennine	Gran Sasso	42°27'	13°36'	2912		1750	14C	*(S21,31)*
	Apennine	S Apennine	40°07'	15°51'	2267		1700		*(S31)*
Croatia		Snezniska Planota	45°35'	14°27'	1643		1400-1500		*(S32)*
		Velebit	44°21'	15°30'	1686		1200-1300		*(S32)*
Bosnia		Plocna	43°36'	17°35'	2228		1900-2000		*(S32)*
		Prenje	43°33'	17°54'	2155		1500		*(S32)*
Mte Negro		Veliko Vetao	43°13'	18°45'	2396		1600		*(S32)*
		Durmitor	43°08'	19°03'	2522		1800		*(S32)*
		Orjen	42°34'	18°32'	1894		1300		*(S33, 34,35)*
Albania		Shara Range	42°02'	20°52'	2748		2000		*(S35)*
		E Albanian Alps	42°32'	20°08'	2656		1650		*(S35)*
		W Albanian Alps	42°23'	19°48'	2693		1500		*(S21,36)*
		Albanian Mtns	41°45'	20°14'	2767		1600		*(S21,36)*
Greece	W-Greece	Smolikas/Tymphi	40°01'	20°52'	2637		2200-1700	U-Th	*(S21,36,37)*
		Helmos	37°58'	22°12'			1900		*(S21,36)*
		Taigetos	37°06'	22°18'	2407		2000		*(S21,36)*
	E-Greece	Olymp	40°05'	22°21'E	2917		2200-1900		*(S37)*
	Crete	Psiloriti (Ida)	35°13'	24°47°	2500		2500		*(S32)*
Romania	S Carpathians	Fagarasi	45°30'	23°40'E	2535		1900		*(S32)*
	S Carpathians	Retezat	45°20'	23°35'E	2502		1800	10Be	*(S38)*
N-Africa	High Atlas	Jbel Toubkal	31°03'	7°57'W	4165		3500		*(S37)*
		Irhil M'Goun	31°30'	6°27'W	4070		3400		*(S37)*
		Jbel Ayachi	32°29'	4°56'W	3751		3300		*(S37)*
	Middle Atlas	Jbel Bou Iblane	33°41'	4°03'W	3340		2400-2500		*(S37)*
		Jbel Bou Naceur	33°33'	3°54'W	3310				*(S37)*
	Saharan Atlas	Djurdjura	36°28'	4°08'E	2308		1900-2100		*(S32)*

References of Table S2:

S22 A. Pérez Alberti, M. Valcárel Díaz, R. Blanco Chao, in J. Ehlers, P.L. Gibbard (Eds.), *Quaternary Glaciations – Extent and chronology Part I. Europe* **2**, 389 (2004)

S23 M. Calvet, M., in J. Ehlers, P.L. Gibbard, (Eds.), *Quaternary Glaciations – Extent and chronology Part I. Europe* **2**, 119 (2004)

S24 J.-L. Mercier, M. Jeser, in J. Ehlers, P.L. Gibbard (Eds.), *Quaternary Glaciations – Extent and chronology Part I. Europe* **2**, 113 (2004)

S25 B. Etlicher, *Bull. de l'Assoc. Française pour l'Etude du Quaternaire* **2/3**, 117 (1985)

S26 J.-F. Buoncristiani, M. Campy , in J. Ehlers, P.L. Gibbard (Eds.), *Quaternary Glaciations – Extent and chronology Part I. Europe* **2**, 111 (2004b).

S27 J.-F. Buoncristiani, M. Campy , in J. Ehlers, P.L. Gibbard (Eds.), *Quaternary Glaciations – Extent and chronology Part I. Europe* **2**, 101 (2004a).

S28 H. De Goër, *Ann. Faculté Sci. de Clermont-Ferrand*, **48**, 204 pp. (1972)

S29 Y. Veyret, thèse, Presse universitaire de Lille, 2 Vol.: 783 pp. (1981)

S30 C. Benz, thesis Phys. Geogr., Univ. Zurich **43**, 180 pp. (2003)

S31 C. Giraudi, in J. Ehlers, P.L. Gibbard, (Eds.), *Quaternary Glaciations – Extent and chronology Part I. Europe* **2**, 21 (2004)

S32 B. Messerli, B. *Geogr. Helv.* **22**, 105 (1967).

S33 J. Cvijic, *Glas Srpske Kraljevske Akademije Nauka*, **LVII**, 1-196, Belgrade (1899)

S34 M. Markovic, thesis, 285 pp., Faculty of Mining and Geology, Belgrade (1973)

S35 L. Menkovic et al. 2004. in J. Ehlers, P.L. Gibbard, (Eds.), *Quaternary Glaciations – Extent and chronology Part I. Europe* **2**, 379 (2004)

S36 J.C. Woodward, M.G. Macklin, G.R. Smith, G.R. in J. Ehlers, P.L. Gibbard (Eds.), *Quaternary Glaciations – Extent and chronology Part I. Europe* **2**, 155 (2004)
S37 P.D. Hughes, P.L. Gibbard, J.C Woodward, J.C. In: J. Ehlers, P.L. Gibbard (Eds.), *Quaternary Glaciations – Extent and Chronology, Part III: South America, Asia, Africa, Australia, Antarctica*, 255 (2004)
S38 A. Reuther et al., *Quaternary International* **164**, 151 (2007).

Data supplement 3: Mediterranean ELA and temperature depression

Figure S5 shows a map comparing the modern ELA with that of the LGM (S2; Figure 1), and the elevation difference between them, which is shown in Figure 2. Note that the modern and ancient ELA positions are by necessity estimated above the Mediterranean Sea, which therefore applies also to the elevation difference. The isolines of elevation differences roughly follow the ELA lines of the LGM above the Mediterranean Sea, whereas Messerli *(S13)* plotted a quite straight east-west orientation of ELA isolines. The difference in elevation is combined with a mean free atmospheric lapse rate of 6.5 °C km^{-1} to calculate the temperature depression during the LGM in altitudes of 1 to 3 km (Figure 2). Note that this calculation is an end-member scenario applied only to achieve comparison with SST, and provides an apparent temperature anomaly pattern which is in fact indicative of precipitation anomalies.

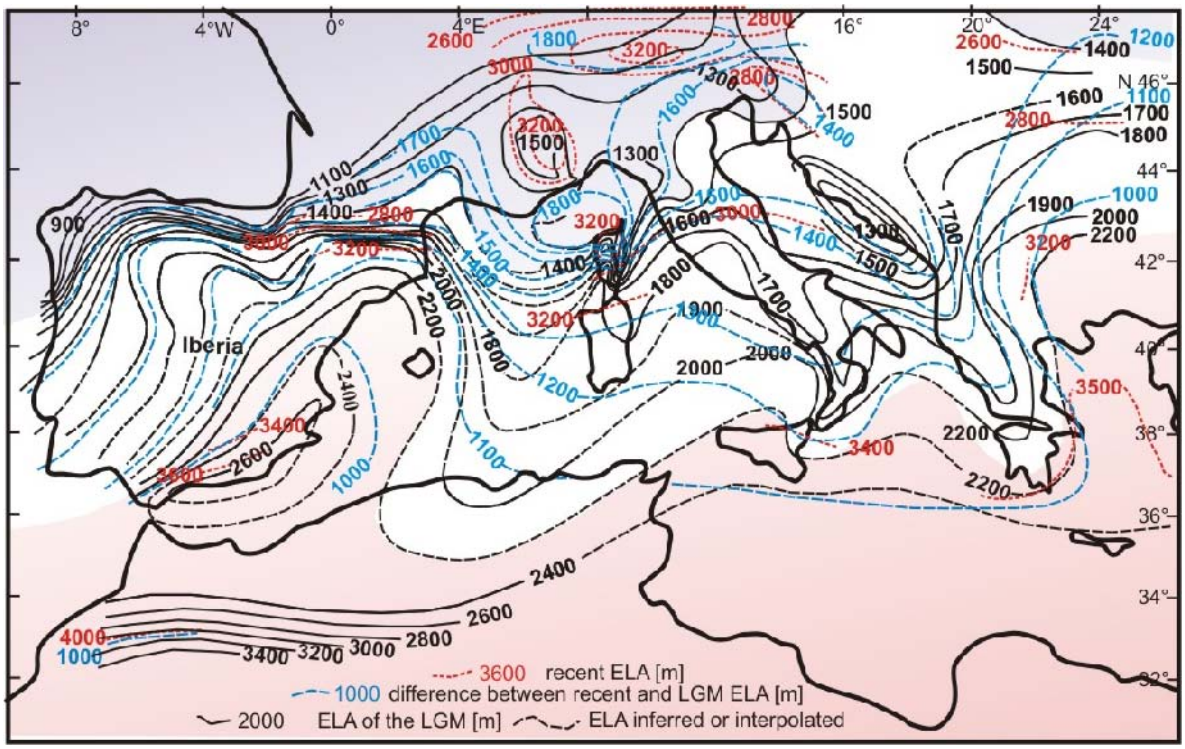

Figure S5: Comparison of the ELA at Present with that of the LGM, used to construct the ELA depression

Fig S6 refers to Hayes et al. (*S39*), who compare recent and LGM SSTs on a similar scale. The isolines displayed in their maps have been subtracted from another to obtain the cooling during the LGM relative to the present (Figure 2). The map in Fig. S6 is shown to illustrate that the general pattern of the LGM and the present are controlled by basin geometry and prevailing winds.

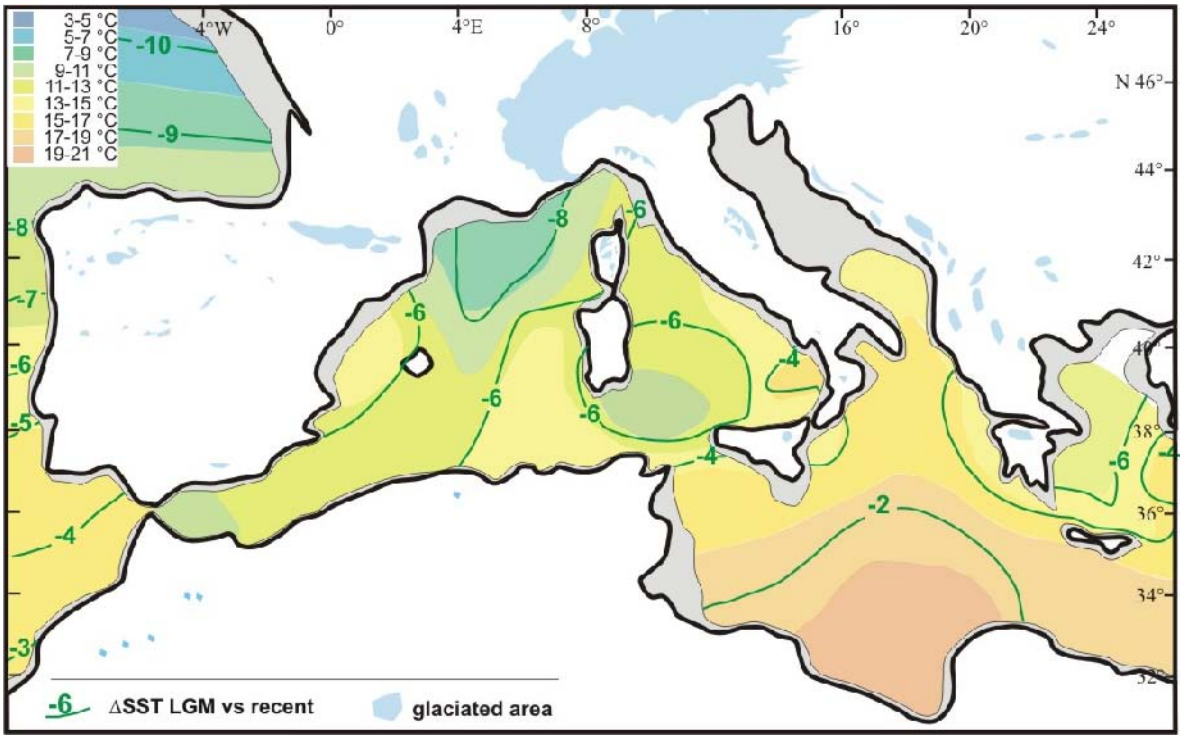

Figure S6: Annual average SST in the LGM, and the SST depression as compared to the Present, shown as green isolines

The temperature differences calculated from glacial ELA depression, relative to the present, generally agree with lower-altitude temperature reconstructions from palaeofloral data (*S39, S40*). This is particularly true for the sites in southeastern Europe (Fig. 2).

In south-central Italy, the two palaeoflora temperature estimates do not (within error) overlap between minus 7 to 9 °C of relative cooling and are thus inconsistent. In this region, the temperature equivalent of the ELA depression at higher elevation indicates about minus $8.7^{\pm 1}$ C.

Further to the south, both land temperature depressions are close and indicate warmer land conditions than indicated by the ELA at higher elevation. Since the SST depression is only 5 °C in this region, causing a significant warm SST anomaly (Fig. 2, main paper), we infer that the warmer palaeoflora temperature estimate (*S40*) is realistic, and infer a locally enhanced convective precipitation in this area (main paper).

In the Rhône valley, all estimates agree well, reflecting relatively cold conditions, in line with dominant northerly winds. Possibly, katabatic winds from the Alpine glaciers contributed to exceptionally cold conditions in the Rhône valley. Slightly warmer land temperatures NW of the Alps as compared to the ELA temperature estimate may reflect favourable local conditions, not affected by katabatic winds. On the southern flank of the French Massif Central, land temperature depressions are somewhat lower than those indicated by the ELA (*S39*), but still close (*S40*). The local cooling trend towards the Rhône valley is evident in all data.

In NW Iberia, land temperatures are significantly warmer than the ELA temperature depression. We infer that this region was affected by warm waters of the Gulf Stream (Fig. 2, main text), which would mean that locally enhanced convective precipitation partly accounted for the regional ELA depression in NW Iberia. In SW France, the various land

temperature estimates are in conflict. Possibly, SW France was also affected by the Gulf Stream influences, albeit to a lesser degree.

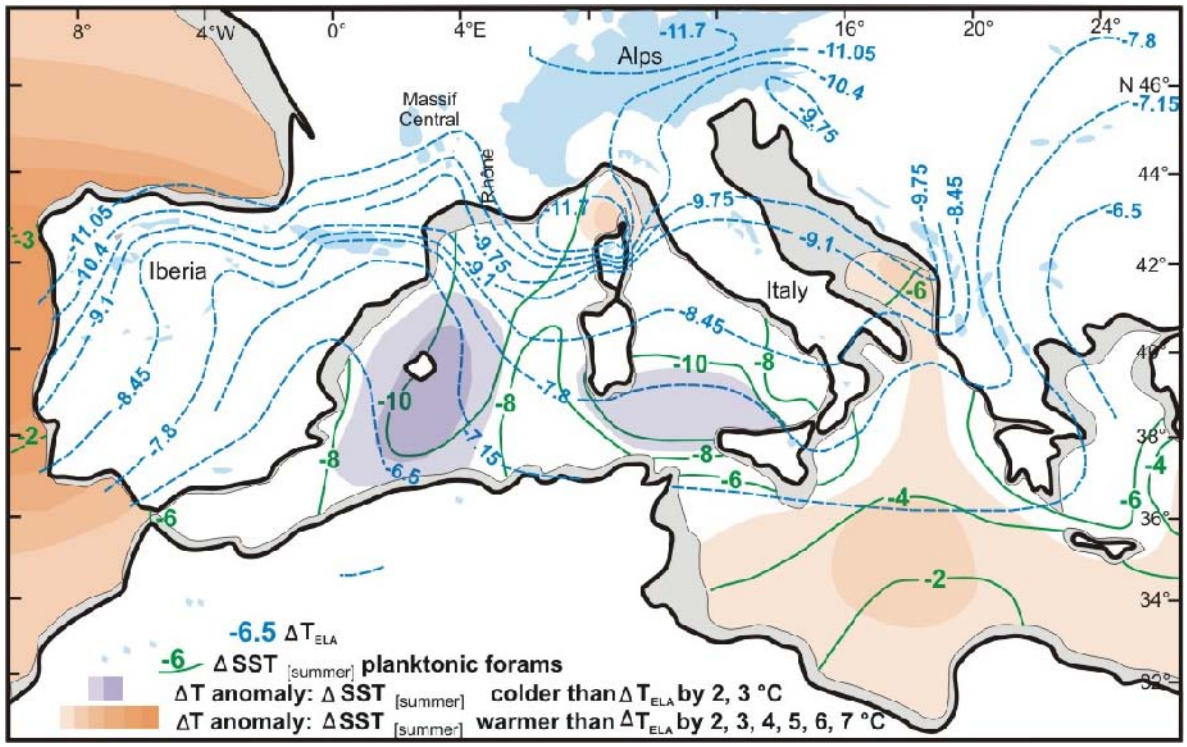

Figure S7: Modified plot of Figure 2 (main paper), using summer Δ SST *(S39, S42)* instead of annual average Δ SST.

We have compared annual averages of SST depression with the ELA depression in the main paper, although a comparison with summer SST seems to be more appropriate at Present, since the air temperature in the melting season appears to govern the ELA (*S6;* Figure S7). We found, however, that the relationship of the ELA with summer air temperature is modified by cloudiness, spring rainfall/snowfall depending on short-term synoptic conditions, surrounding host rock, and other parameters. A plot of summer SST depression relative to the ELA depression (Figure S7), generated similarly to Figure 2, exposes the same pattern of regional gradients in the Mediterranean, but shows cold anomalies around and south of the Balearic Islands, and between Sardinia and Sicily. The latter anomaly might be explained by leeward upwelling due to persistent NW winds, which are attested by the geometry of fossil dunes in Sardinia and relatively cool SSTs (Figure S6). The cold anomaly around the Balearic Islands, however, is in conflict with both summer and annual average SST in the LGM (*S41*). We cannot reasonably explain such a cold anomaly by oceanographic processes in the given setting. Moreover, such cold conditions would favour stable stratification of the lower atmosphere, which would have caused regionally enhanced aridity, for which no evidence exists. For unclear reasons, the annual average SST pattern in the LGM is more reasonable for a comparison with the ELA. This applies also to east Atlantic SST off Iberia (*42*), where summer SST values are unreasonably high when compared to the ELA end-member temperature depression.

There is an apparent conflict between zonal versus meridional circulation arguments on the one hand, and typical weather regimes on the other, which cannot be resolved for the LGM on the basis of currently available data. A detailed discussion of this issue goes beyond the scope of this paper, but we do briefly address it in the following.

As noted in the main paper, our data do not support a zonal LGM atmospheric circulation. However, frequent distinctly meridional circulation during cold seasons (as illustrated by the LGM ELA pattern) may have alternated with zonal circulation during warm seasons, which in the average of the LGM year may have even been the dominant mode, as inferred from climate models. In such a scenario, there would be no conflict between models and paleo-data, and for a better understanding a synoptic approach would be required with simplified typical weather regimes.

With an LGM polar front on average located further south *(43),* southeast-directed passage of polar front cyclones and their perturbations into the Mediterranean would cause outbreaks of polar air into the Gulf of Lions more frequently than at Present *(S44)*. Such cyclone tracks are not easily compatible with the previously suggested SW-directed pressure ridge of the Scandinavian Mobile Polar High towards southern Iberia *(S45)*. Both suggestions, however, might be compatible if they each prevailed for only part of the year.

Our reconstruction favours considerable cyclonic activity in the western Mediterranean during the LGM, but we do not suggest a zonal route for the storms across the basin as a result of a zonal regime. We suggest more frequent local cyclone generation north of Corsica (Gulf of Genoa), particularly in winter and spring. Today, fast-moving Atlantic cyclones and disturbances rush through the Mediterranean basin and cause moderate precipitation that increases with elevation. By contrast, regionally generated Genoa cyclones move slowly and even become stationary. They are typically associated with strong local convective precipitation and sharp horizontal precipitation gradients, like those shown in Fig. S4.

Progress both with proxy-based palaeoclimate reconstruction and climate modelling hinge on seasonal particularities. SST proxy data from foraminiferal assemblages are considered to indicate annual as well as seasonal averages (S*41*), whereas geochemical SST proxies represent the season of maximum growth of the proxy carrier, which may even not have been the same in the past as in the present for the individual plankton groups. Palaeoflora is typically indicative of annual average temperatures and the coldest month (*S39,40*). The ELA is generally assumed to be indicative of the summer temperature (*S6*), but this seasonal attribution may vary regionally depending on the seasonality of precipitation. As discussed in S1, springtime snowfall may have played an important role for the ELA patterns on Corsica. The seasonal pattern of LGM precipitation is even more difficult to handle. Our approach of interpreting paleodata in terms of dominant weather regimes in analogy to the Present and the Little Ice Age provides a conceptual, hypothesis generating method, presenting one way of bridging the gap from the information contained in the multi-year averages of paleoproxy data to the understanding of the weather systems responsible for long-term climate trends.

References:

S39 O. Peyron *et al., Quat. Res.* **49**, 183 (1998)
S40 H. Wu, J. Guiot, S. Brewer Z. Guo, *Clim. Dyn.* **29**, 211–229 (2007)
S41 A. Hayes, M. Kucera, N. Kallel, L. Sbaffi, E.J. Rohling, *Quat .Sci .Rev.* **24**, 999–1016 (2005)
S42 M. Kucera, *et al.*, *Quat. Sci. Rev.*, **24**, 951–998 (2005).
S43 COHMAP Members, *Science* 241, 1043 (1988)
S44 M. Kageyama, F. D. Andrea, G. Ramstein, P.J. Valdes, R. Vautard, *Clim. Dyn.* **15**, 773-793 (1999)
S45 M.F. Sánchez-Goni *et al.*, *Climate Dyn.* **19**, 95 (2002).